

Towards fast machine-learning-assisted Bayesian posterior inference of realistic microseismic events

Davide Piras^{1*}, Alessio Spurio Mancini^{1,2,3}, Benjamin Joachimi¹, Michael P. Hobson³

¹Department of Physics and Astronomy, University College London, Gower Street, London, WC1E 6BT, UK

²Mullard Space Science Laboratory, University College London, Holmbury St. Mary, Dorking, Surrey, RH5 6NT, UK

³Astrophysics Group, Cavendish Laboratory, J. J. Thomson Avenue, Cambridge, CB3 0HE, UK

14 January 2021

SUMMARY

Bayesian inference applied to microseismic activity monitoring allows for principled estimation of the coordinates of microseismic events from recorded seismograms, and their associated uncertainties. However, forward modelling of these microseismic events, necessary to perform Bayesian source inversion, can be prohibitively expensive in terms of computational resources. A viable solution is to train a surrogate model based on machine learning techniques, to emulate the forward model and thus accelerate Bayesian inference. In this paper, we improve on previous work, which considered only sources with isotropic moment tensor. We train a machine learning algorithm on the power spectrum of the recorded pressure wave and show that the trained emulator allows for the complete and fast retrieval of the event coordinates for *any* source mechanism. Moreover, we show that our approach is computationally inexpensive, as it can be run in less than 1 hour on a commercial laptop, while yielding accurate results using less than 10^4 training seismograms. We additionally demonstrate how the trained emulators can be used to identify the source mechanism through the estimation of the Bayesian evidence. This work lays the foundations for the efficient localisation and characterisation of any recorded seismogram, thus helping to quantify human impact on seismic activity and mitigate seismic hazard.

Key words: seismograms – microseismicity – statistical methods – seismic modelling – artificial intelligence.

1 INTRODUCTION

Underground human activity, including fluid injection in rocks and mining operations, can cause seismic events with much smaller amplitude than large-scale earthquakes (Majer et al., 2007; Ellsworth, 2013). These induced seismic signals are usually referred to as microseismic events, and their monitoring is critical in understanding the impact of human activity on seismic hazard (Brueckl et al., 2008; Shapiro et al., 2010; Mukuhira et al., 2016; Das et al., 2017, and references therein). Microseismic events are usually tracked by placing geophones on the land surface or at the seabed (Panahi et al., 2005; Fertitta et al., 2010). Besides measuring the amplitude of the seismograms, these sensors allow for a spatial and temporal localisation of the event. In particular, once a seismogram has been recorded, we wish to infer its source location in the subsurface, in order to mitigate the seismic hazard and forecast seismic risk.

Various methods for microseismic event - and, more generally, earthquake - location are available in the literature, dating back to the work of Geiger (1910), and up to today (see e.g. Vasco et al., 2019, and references therein, for a recent review). One of

the most common approaches relies on estimating the first arrival time by means of the eikonal equation (see e.g. Noack and Clark, 2017; Smith et al., 2020), which allows for the direct comparison of travel times through a direct grid search or more sophisticated techniques (Wuestefeld et al., 2018). More accurate predictions can be obtained exploiting methods that take into consideration the full waveform, even though they generally require more computational resources (Angus et al., 2014; Vasco et al., 2019).

A Bayesian approach can be adopted to solve the inverse problem as well (Lomax et al., 2000; Tarantola, 2005; Stähler and Sigloch, 2014, 2016; Pugh et al., 2016). We assume a model where each microseismic event is uniquely identified by a set of coordinates, which are the model parameters. Then, given a seismogram, we wish to obtain the parameters' posterior distribution, which is used to provide an estimate of the model parameters and their associated uncertainty. Markov Chain Monte Carlo (MCMC; see e.g. Craiu and Rosenthal, 2014, for a review) and nested sampling (Skilling, 2006) techniques are among those employed to sample the posterior distribution. However, this approach becomes prohibitive when dealing with a high number of parameters, or when the forward model is computationally expensive to simulate (see e.g. Rajaratnam and Sparks, 2015; Conrad et al., 2016; Alsing

* d.piras@ucl.ac.uk

et al., 2018). For these reasons, being able to cheaply and accurately simulate a microseismic event given its coordinates has become paramount in recent years. In order to obtain forward simulations of microseismic events, one must solve the elastic wave equation given a 3-D heterogenous density and velocity model for the propagating medium (Das et al., 2017), which can be prohibitively expensive unless sophisticated techniques are implemented.

Machine-learning generative models have gained considerable attention in recent years, with applications to many fields ranging from computer vision (Goodfellow et al., 2014; Gulrajani et al., 2016) to astrophysics (Auld et al., 2007, 2008), as well as climate science, nuclear physics and drug selection (see e.g. Kasim et al., 2020; Chenthamarakshan et al., 2020). These advances have been enabled by both an increased accessibility to specific computational resources, as well as a significant growth in the amount of available data.

In geophysics, Das et al. (2017) developed an optimised approach to microseismic events generation that, for each set of coordinates and given a physical model for the propagating medium, produces the corresponding seismogram in $\mathcal{O}(1 \text{ h})$ using a Tesla graphics processing unit (GPU) and the software K-WAVE (Treeby et al., 2014). Subsequently, Das et al. (2018) and Spurio Mancini et al. (2020) (D18 and SM20 hereafter, respectively) showed the limitations of this direct approach, and presented an alternative where the mapping is learnt using machine learning techniques. In particular, D18 showed how Gaussian Processes (GPs, Rasmussen and Williams, 2005) can be used to learn an accurate surrogate model, while SM20 demonstrated the effectiveness of a variety of machine learning algorithms as emulators, and showed how their surrogate model yields an accurate estimate of the posterior distribution of an event’s coordinates in a fraction of the time required by the D18 method.

D18 and SM20, however, only applied their methodologies to isotropic microseismic events. It is well known that any source mechanism can be mathematically decomposed into three components: isotropic (ISO), double couple (DC), and compensated linear vector dipole (CLVD) (see e.g. Knopoff and Randall, 1970; Vavryčuk, 2001, 2005; Vavryčuk, 2015). The pure ISO source is associated with implosive or explosive force, while the pure DC source is caused by shear faulting. The CLVD source is coupled to the ISO source, but compressive stress is exerted along one direction, while tensile stress is exerted along the other two (Li et al., 2015).

In this paper, we present an approach that aims at learning the direct mapping between coordinates and seismograms for any microseismic source type (ISO, DC and CLVD). We show that it is sufficient to consider the power spectrum of the recorded pressure waves in order to distinguish different seismograms, and we train a simple machine learning algorithm to learn this mapping efficiently. Moreover, we demonstrate how our method allows for the accurate inference of the posterior distribution of the coordinates of a single source in $\mathcal{O}(0.1 \text{ h})$ on a commercial laptop, thus paving the way for the fast and inexpensive localisation of *any* microseismic event. Finally, we show how we can use the trained emulators to identify the source mechanism through Bayesian evidence estimation, thus demonstrating the versatility of our Bayesian approach.

We structure the paper as follows. In Sect. 2 we describe the data we consider in this work. In Sect. 3 we explain what preprocessing steps we perform and briefly recall the details of the generative method we employ. We show its performance at both training and inference time in Sect. 4. Finally, in Sect. 5 we discuss our results and provide an outlook on possible extensions of this work.

2 DATA

In this work, we consider the same data framework as D18 and SM20, starting from 3-D heterogenous density and velocity models for the propagating medium, which we show in Fig. 1. The model, which is discretised on a 3-D grid of voxels, specifies the values of the density ρ of the propagating medium, as well as the propagation velocities for P- and S-waves (V_p , V_s). We assume that sensors are placed at the seabed, and that they record both pressure and three-component particle velocity of the propagating medium (even though we will use only the former, as we explain later on). As anticipated, our aim is to apply our method to any source mechanism, so we will consider a more general generation procedure than previous work. Unlike D18 and SM20, who only considered isotropic sources, we take the microseismic moment tensor to be one of three types, which we denote as \mathbf{M}_{ISO} , \mathbf{M}_{DC} and \mathbf{M}_{CLVD} . Following Vavryčuk (2005) and Li et al. (2015), we define these quantities as:

$$\mathbf{M}_{\text{ISO}} = \begin{bmatrix} M_{11} & 0 & 0 \\ 0 & M_{22} & 0 \\ 0 & 0 & M_{33} \end{bmatrix}, \quad (1)$$

$$\mathbf{M}_{\text{DC}} = \begin{bmatrix} 0 & M_{12} & 0 \\ M_{21} & 0 & 0 \\ 0 & 0 & 0 \end{bmatrix}, \quad (2)$$

$$\mathbf{M}_{\text{CLVD}} = \begin{bmatrix} M_{11} & 0 & 0 \\ 0 & M_{22} & 0 \\ 0 & 0 & -2M_{33} \end{bmatrix}, \quad (3)$$

where each M_{ij} represents a different couple of forces. We additionally assume $M_{11} = M_{22} = M_{33} = M_{12} = M_{21} = 1 \text{ MPa}$, which is a realistic assumption following Collettini and Barchi (2002). In practice, isotropic (ISO) events are characterised by a single (explosive or implosive) P-wave, while double couple (DC) events are linked to shear stress and are characterised by both a P- and S-wave, with comparable amplitudes. Similarly to isotropic events, compensated linear vector dipole (CLVD) events display an often dominant principal wave, whose amplitude is however much smaller than the isotropic one, and a non-negligible S-wave.

We generate forward simulations using the GPU implementation of Das et al. (2017), separately using 4 types of GPUs: Tesla K20, Tesla C2075, GeForce RTX 2080 Ti and GeForce GTX 1080 Ti. For each source type, we produce 10000 events corresponding to different source locations, which are randomly sampled using Latin Hypercube Sampling on a 3-D grid of $81 \times 81 \times 301$ points, corresponding to a real geological model of size $1 \text{ km} \times 1 \text{ km} \times 3 \text{ km}$. The total time to generate these data using the hardware specified above is about 150 h for each source type. We consider 23 receivers in total, whose position is depicted in Fig. 2, even though we stress that we will not focus on finding the optimal geometry of the sensors in this work. In Sect. 4.2 we will present the results of a full analysis of the dependence of the posterior distribution on the number of training points, the number of receivers and the noise level, in order to demonstrate the robustness of our approach.

The temporal resolution for the solution of the elastic wave equation is 0.5 ms (2 kHz), and the total length of each seismic event is 5 s. After generation, all seismograms are downsampled to a time resolution of 2.5 ms (400 Hz) to reduce computational storage; this is done by keeping only the first of each group of 5 components. In this way, each seismic trace is ultimately a time series composed of $N_t = 2001$ time components: we show an example for each source mechanism in the left column of Fig. 3.

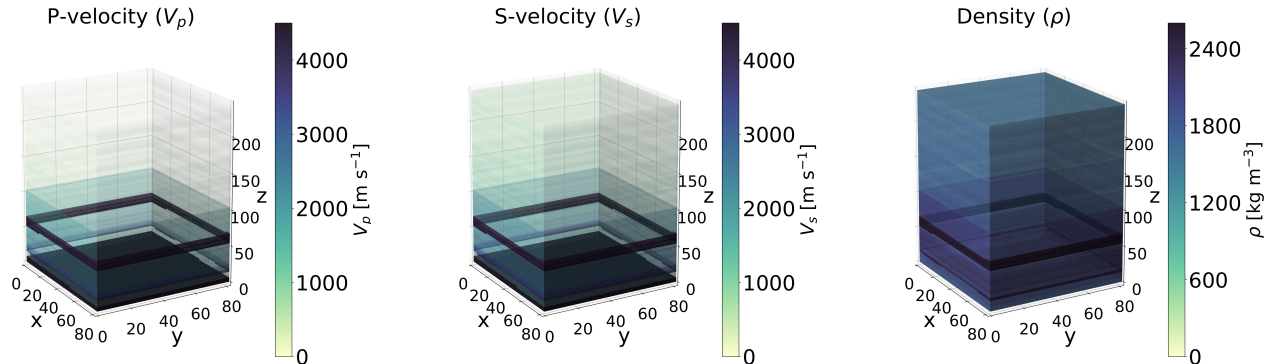


Figure 1. P-wave velocity (V_p), S-wave velocity (V_s) and density (ρ) models of the simulated domain we consider in this work. The models are specified as 3-D grids of voxels, with size $81 \times 81 \times 301$ points, corresponding to a real geological model of size $1 \text{ km} \times 1 \text{ km} \times 3 \text{ km}$. We observe that our model has a layered structure, with variation along the vertical dimension more marked than along horizontal planes. The plots were adapted from figure 1 in [Spurio Mancini et al. \(2020\)](#).

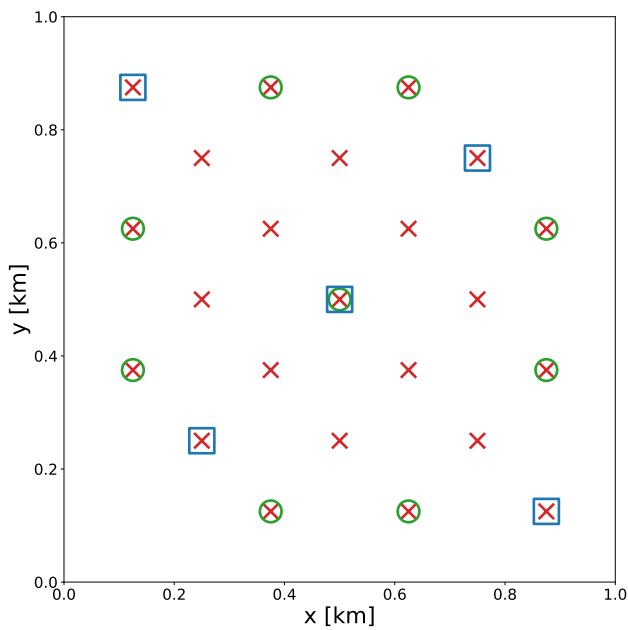


Figure 2. Projection of the positions of the 23 receivers on the $x - y$ plane; $z = 2.43 \text{ km}$ corresponds to the seabed, where all sensors lie. Each receiver records the acoustic pressure wave and particle velocity generated by a microseismic event below the seabed. The red crosses indicate all 23 receivers, while green circles and blue squares (9 and 5 receivers, respectively) refer to subsets of receivers we used to test the robustness of our method, as shown in Sect. 4.2.

Finally, note that we consider the seismograms to be noiseless at training time, while some noise is added to the simulated recorded event when performing inference on the coordinates' posterior distribution. We will discuss and show the effect of the noise level in Sect. 3.1 and Sect. 4.2, respectively.

3 PREPROCESSING, GENERATIVE MODEL AND INFERENCE

3.1 Preprocessing

Learning a mapping between coordinates and seismograms directly would be hard for at least two reasons. First, each signal has features with different amplitudes: this means that e.g. a neural network (which will be described in detail in Sect. 3.2) would likely just focus on the main peak and ignore the other components, thus losing useful information for the localisation purpose. Secondly, given the complexity of the seismograms and the high number of features, the amount of data required to train an accurate emulator without overfitting would be at least an order of magnitude higher than what we consider in this work (see e.g. [Bishop, 2006](#); [Zhu et al., 2015](#), and references therein).

In this sense, we *have to* preprocess the seismograms in order to extract only the relevant information that is needed to localise an event, while discarding all the noisy or redundant features of the signal. Both D18 and SM20 showed the importance of preprocessing, employing GPs in order to select only the components of each seismogram that are essential for inference. However, their methods fail on more complicated sources like the ones we consider in this work. While it could be argued that employing more training data could improve the results, it is also well-known that GPs do not scale well with the number of training points ([Liu et al., 2018](#)), thus it is likely that the D18 method would struggle to generalise to more complicated source mechanisms. Additionally, the method proposed in SM20 is applied directly to the complicated seismic traces like the ones in the left panel of Fig. 3, thus making it more difficult for any algorithm to capture the most useful features for localisation. Therefore, we follow a different preprocessing procedure, based on translating the data to the Fourier domain, and we outline the steps in the next paragraphs.

The left panel of Fig. 4 shows the mean and standard deviation of all seismograms in the training set (8000 seismic traces - see Sect. 3.2 for more details): based on these distributions, we keep all components of the DC and CLVD signals, and only keep the first half of the ISO traces. In other words, we keep only $N_{\text{keep}} = 1000$ time components for the ISO traces, and $N_{\text{keep}} = N_t = 2001$ time components for the other mechanisms.

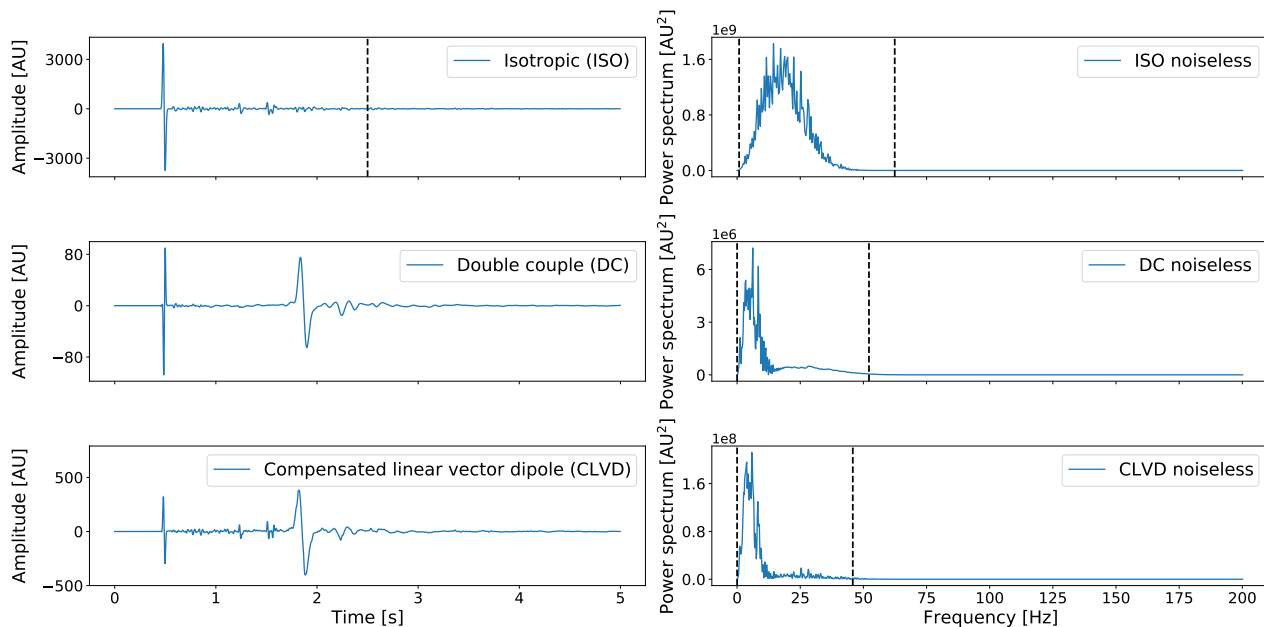


Figure 3. *Left column:* Example acoustic pressure wave for each different type of moment tensor: isotropic (ISO), double couple (DC) and compensated linear vector dipole (CLVD). These seismograms correspond to a source location of $(x, y, z) = (0.55 \text{ km}, 0.73 \text{ km}, 1.8 \text{ km})$ as recorded by a receiver in $(x, y, z) = (0.13 \text{ km}, 0.38 \text{ km}, 2.43 \text{ km})$. The seismograms’ amplitude is measured in arbitrary units of pressure. Note the different scales for each source mechanism. The dashed black line in the top panel indicates a cut we perform for the isotropic sources only, based on the left panel of Fig. 4. *Right column:* The corresponding power spectra, calculated as described in Sect. 3.1. No noise is added when training the emulator, while some noise is introduced when doing inference, as described in Sect. 3.3. The dashed lines indicate a frequency cut we perform to further reduce the number of features and to be robust to noise, based on the right panel of Fig. 4.

The next preprocessing step we implement is applying the one-dimensional discrete Fourier Transform (Cooley and Tukey, 1965) to each seismogram, using the version of NUMPY[†]. Since the amplitudes at each time component are real numbers, the Fourier Transform returns $(\lfloor N_{\text{keep}}/2 \rfloor + 1)$ frequency components: this means that for DC and CLVD sources we are left with 1001 components (501 in the ISO case) in the Fourier domain. We then take the square of the absolute value of these complex numbers: this is usually referred to as a power spectrum. In the right column of Fig. 3 we report the power spectra corresponding to the seismograms in the left column of the same figure. We further take the decimal logarithm of the power spectra at each frequency value, and refer to it as logarithmic power spectra in the rest of the paper.

As anticipated, we shall add some noise to the observed seismogram whose coordinates will be inferred. In the right panel of Fig. 4 we show the mean power spectra for each source mechanism with and without noise, which will be described in detail in Sect. 3.3. We calculate the ratio between the noiseless and the noisy signals, and filter out the frequencies for which this ratio is less than 0.99. We experimented with different thresholds, and chose 0.99 as a good balance between retaining enough features to locate a seismogram and being insensitive to noise. In other words, we additionally cut each power spectrum in the ranges [1 Hz, 62.4 Hz], [0 Hz, 52.2 Hz] and [0 Hz, 45.8 Hz] for ISO, DC and CLVD, respectively, to keep the parts of each signal that are less affected by noise. We observe that translating the seismograms to the Fourier domain has allowed us to obtain smoother signals, as well as to

reduce the number of features by a factor of 10. Moreover, this allows our proposed method to be robust to noise: any effect due to noise can be translated into some information of the noise power, and hence accounted for in the analysis. We will discuss this further in Sect. 3.3.

To further reduce the number of features, we apply Principal Component Analysis (PCA). PCA is a standard linear compression technique where the data is projected along the eigenvalues of the data covariance matrix. Considering only the components that carry more variance (the so-called ‘principal components’, corresponding to the largest eigenvalues), it is possible to reduce the number of features while maintaining the relevant information for inference. We fit PCA to the training data, and use it to compress the whole dataset. After applying PCA to the logarithmic power spectra, we retain 10 principal components for each signal. We verified experimentally that varying the number of retained PCA components does not impact the final results significantly.

3.2 Generative model

The following step consists of learning the mapping between coordinates and principal components by means of a neural network (NN). A neural network is a set of subsequent layers, each made of a certain number of neurons, that allow for the parametrisation of any measurable function between finite dimensional spaces (Hornik et al., 1989). Each neuron is associated to a weight, and each layer is additionally associated to a bias (i.e. an offset): weights and biases constitute the parameters that we wish to learn. Additionally, activation functions can be introduced after each layer to model non-linear mappings. Training the neural network consists

[†] <https://numpy.org/doc/stable/reference/routines.fft.html>

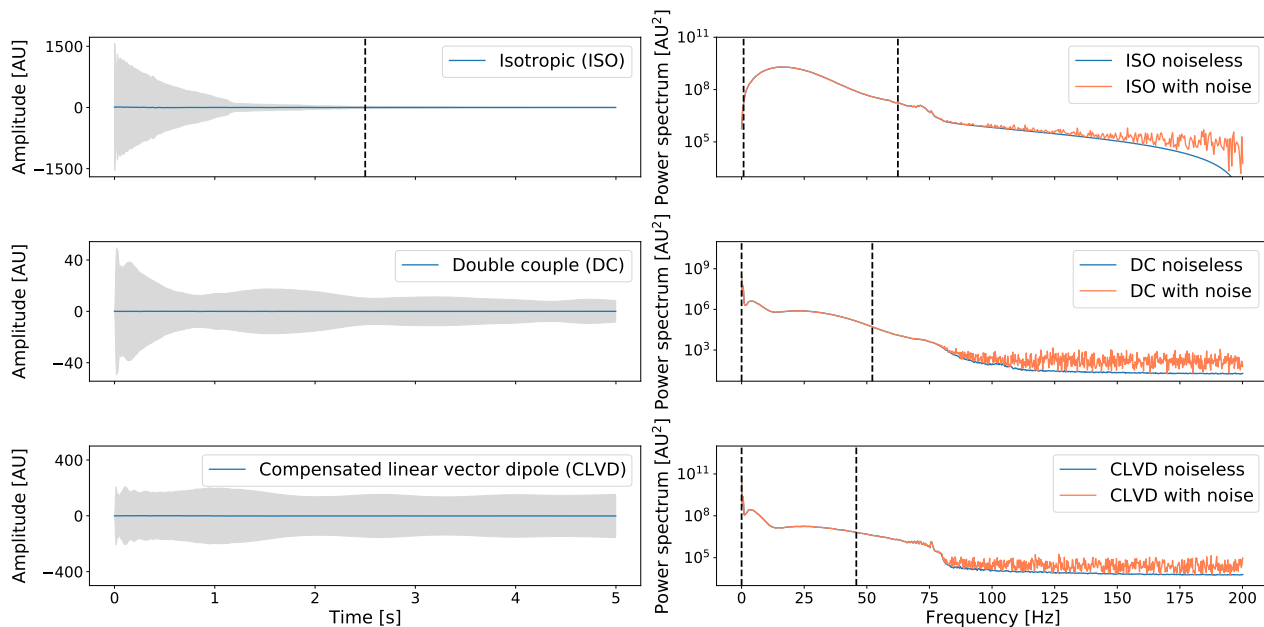


Figure 4. *Left column:* Mean (blue line) and standard deviation (grey area) of all the seismic traces in the training set, for each source mechanism: isotropic (ISO), double couple (DC) and compensated linear vector dipole (CLVD). The seismograms’ amplitude is measured in arbitrary units of pressure. The training set is made of 8000 traces for each source mechanism. We cut the isotropic sources at 2.5 s, as indicated by the dashed black line. *Right column:* Noiseless (blue) and noisy (coral) mean of the corresponding power spectra, calculated as described in Sect. 3.1. We consider a signal-to-noise ratio of 33 dB, as described in Sect. 3.3. We filter the power spectra between the dashed lines selecting only the frequencies where the ratio between the noiseless and noisy signals is more than 99%.

of feeding some data through all the layers, and then updating the value of the parameters in order to optimise a chosen loss function.

Our goal is to learn a mapping between coordinates and principal components. We employ a neural network made of three layers with 256 neurons each, to provide enough flexibility to the parametrisation without consuming too much memory. We set Leaky ReLU (Maas et al., 2013) as the activation function for all layers except the last one, where we keep a linear activation function. We recall here that Leaky ReLU acts on the output of each layer \mathbf{O} as follows:

$$\text{LeakyReLU}(\mathbf{O}) = \begin{cases} \mathbf{O} & \text{if } \mathbf{O} > 0 \\ \alpha\mathbf{O} & \text{otherwise} \end{cases}, \quad (4)$$

where we set the hyperparameter $\alpha = 0.3$; Leaky ReLU is usually preferred over the standard ReLU (rectified linear unit) because of non-vanishing gradients (Kolen and Kremer, 2001). We choose the Mean Squared Error (MSE) between the network output and the principal components of the training data as our loss function to minimise. We note that the preprocessing steps applied to our logarithmic power spectra correspond to the method ‘PCA+NN’ in SM20.

For each source mechanism and each receiver, we train the emulator using 8000 traces; we reserve 1000 seismograms for validation purposes and 1000 seismograms for testing purposes. To train the neural network, we use the Adam optimiser (Kingma and Ba, 2014) with default parameters; moreover, we choose a learning rate of 0.001 and a batch size of 256: the former controls the step size of the parameters’ update, while the latter indicates the number of training points that are fed through the network at each iteration. We additionally set a patience of 50 to early-stop (Yao et al., 2007) based on the validation loss: this means that if the loss calculated on the validation set has not decreased in the last 50 epochs, we

stop training and take the model corresponding to the minimum validation loss as the best model. The test set is used to randomly sample events on which we perform our Bayesian analysis. We also explore the behaviour of the posterior distribution as a function of the number of training events, number of receivers and noise scale, which we show in Sect. 4.2. However, we do not perform a full grid search amongst the hyperparameters (e.g. number of layers, number of neurons, activation function and learning rate), as we observe the results are not significantly affected by them; we defer a more complete grid search to future work.

3.3 Inference

Once the emulator has been trained, it can be used as the forward model to perform Bayesian inference on the source location of a microseismic event. We recall here the basic assumptions of our Bayesian analysis.

Given a set of parameters θ (the coordinates, in our case), their posterior distribution given some data \mathbf{D} and some hypothesis \mathcal{H} can be written using Bayes’ theorem (see e.g. Bishop, 2006):

$$\Pr(\theta|\mathbf{D}, \mathcal{H}) = \frac{\Pr(\mathbf{D}|\theta, \mathcal{H}) \Pr(\theta|\mathcal{H})}{\Pr(\mathbf{D}|\mathcal{H})}, \quad (5)$$

which expresses the posterior distribution $\Pr(\theta|\mathbf{D}, \mathcal{H})$ as the product of the likelihood $\Pr(\mathbf{D}|\theta, \mathcal{H})$ and the parameters’ prior $\Pr(\theta|\mathcal{H})$, divided by the evidence $\Pr(\mathbf{D}|\mathcal{H})$. For the purposes of inference, we will ignore this last term, as it is just a normalisation factor independent of θ ; however, in Sect. 3.4 we show how the evidence can be used to perform model selection, which is another advantage of working in a Bayesian framework. In order to sample the posterior distribution of the source coordinates, we employ

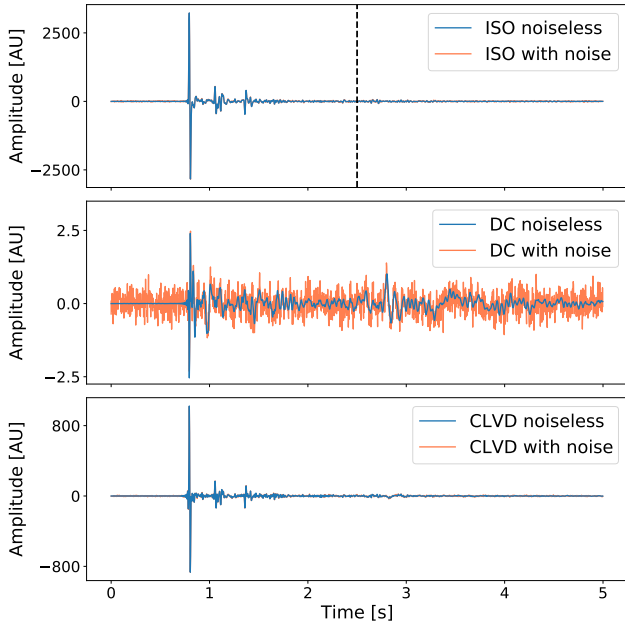


Figure 5. Comparison of the signal without (blue) and with (coral) noise for each source mechanism: isotropic (ISO), double couple (DC) and compensated linear vector dipole (CLVD). As explained in Sect. 3.3, after training the emulator on the noiseless traces, we add Gaussian noise to the observed signal to infer its coordinates. In this case, the seismogram corresponds to event 3 in Table 1 as recorded by a receiver in $(x, y, z) = (0.13 \text{ km}, 0.38 \text{ km}, 2.43 \text{ km})$, and the signal-to-noise ratio (SNR) is 33 dB; we explore higher and lower SNR values in Sect. 4.2 and Fig. 9. The dashed black line in the top panel indicates a cut we perform for the isotropic sources only, based on the left panel of Fig. 4.

nested sampling (Skilling, 2006), as implemented in PYMULTINEST[‡] (Buchner et al., 2014), the Python interface to MULTINEST (Feroz et al., 2009). We choose nested sampling over Metropolis-Hastings sampling or other MCMC techniques as it generally converges faster (Allison and Dunkley, 2014) and provides an estimate of the evidence.

We first randomly choose an event’s coordinates from the test set. For this set of coordinates, we simulate the observation of a microseismic event for each source mechanism, and generate the noiseless trace as it would be recorded by each of the 23 receivers. We add random Gaussian noise to each component of the noiseless trace. We define the signal-to-noise ratio (SNR) as (Li et al., 2018; Zhang et al., 2020):

$$\text{SNR} = 10 \log_{10} \frac{\sum_i^N \sum_j^{N_{\text{keep}}} s_{ij}^2}{\sum_i^N \sum_j^{N_{\text{keep}}} (s_{ij} - \tilde{s}_{ij})^2}, \quad (6)$$

where s_{ij} refers to the j -th component of the i -th trace and \tilde{s}_{ij} to the corresponding noisy trace, $N = 8000$ is the number of training data and $N_{\text{keep}} = 2001$ (1000 in the ISO case) is the number of time components. Following Li et al. (2018), we set SNR= 33 dB, which corresponds to a standard deviation of the Gaussian noise of $\sigma = 10.0, 0.3$ and 3.5 for ISO, DC and CLVD, respectively, in the same arbitrary units as the seismograms’ amplitude. We show examples of noiseless and noisy signals in Fig. 5.

[‡] <https://github.com/JohannesBuchner/PyMultiNest>

We note that the choice of Gaussian noise has a quantifiable consequence on the power spectra of the signals, as it is known that additive white noise has an expected constant power in Fourier space (see e.g. Haykin, 2001; Papoulis et al., 2002). This is reflected on the right-hand side of Fig. 4, where the mean noisy signal is shifted up due to the noise addition. We argue that in general any information about the noise power (even if more complicated than Gaussian noise) can be easily accounted for when preprocessing the data, and this makes our proposed approach robust to noise, as we will show in Sect. 4.2. Moreover, our approach lends itself to the extension to coloured noise, which is most likely in realistic seismic data (Liu et al., 2017).

The noisy seismogram is further preprocessed as described in Sect. 3.1: first, after retaining N_{keep} components, it is translated to the Fourier domain, and the power spectrum is calculated. Then, only the frequencies in the chosen windows are considered, and the decimal logarithm of the power spectrum at each frequency is computed - this is what we refer to as the logarithmic power spectrum. At each likelihood evaluation of PYMULTINEST, the proposed coordinates are mapped to the principal components, and then transformed to the corresponding logarithmic power spectrum. By evaluating the likelihood in multiple points of the prior space, PYMULTINEST can sample from the posterior distribution of the coordinates, thus yielding the required credibility regions in parameter space. Note that, similarly to D18 and SM20, we assume a Gaussian likelihood, without loss of generality as our method can be easily extended to more complicated likelihood models. It is worth stressing that adding Gaussian noise to the seismograms does not necessarily imply that the distribution of the logarithmic power spectra will also be Gaussian; however, we verified experimentally that the distribution of each logarithmic power spectrum component is unimodal and symmetric, thus supporting our assumption.

3.4 Model selection

As detailed in Sect. 3.3, we ignore the denominator in Eq. 5 when inferring the coordinates of a microseismic event. However, we can use the evidence $\Pr(\mathcal{D}|\mathcal{H})$ to perform model selection, thus showing another advantage of our proposed Bayesian approach (see e.g. Knuth et al., 2015). The quantity $\Pr(\mathcal{D}|\mathcal{H})$ can be interpreted as the likelihood of a given signal under a certain hypothesis, with the constraint that the hypotheses form a set of n_{hyp} pairwise disjoint events whose union is the entire possibility space - i.e. $\Pr(\mathcal{H}_i \cap \mathcal{H}_j) = 0$ for $i \neq j$, $\forall i, j = \{1, \dots, n_{\text{hyp}}\}$, and $\sum_{i=1}^{n_{\text{hyp}}} \Pr(\mathcal{H}_i) = 1$.

To compare two hypotheses, and thus perform model selection, we define the Bayes factor BF as:

$$\text{BF} = \frac{\Pr(\mathcal{D}|\mathcal{H}_i)}{\Pr(\mathcal{D}|\mathcal{H}_j)} = \frac{\Pr(\mathcal{H}_i|\mathcal{D}) \Pr(\mathcal{H}_j)}{\Pr(\mathcal{H}_j|\mathcal{D}) \Pr(\mathcal{H}_i)}, \quad (7)$$

where the second equality has been obtained using Bayes’ theorem, $\Pr(\mathcal{H}_i)$ is the prior distribution of the hypothesis \mathcal{H}_i , and $\Pr(\mathcal{D}|\mathcal{H}_i)$ is the posterior distribution of hypothesis \mathcal{H}_i given \mathcal{D} . If the hypotheses are equiprobable *a priori*, we can write $\Pr(\mathcal{H}_i) = \Pr(\mathcal{H}_j)$, which allows us to express the Bayes factor as the ratio of the posterior distribution of one hypothesis over the other. Hence, if the Bayes factor as defined in Eq. 7 is greater than 1, we can interpret it as hypothesis \mathcal{H}_i being more favoured than hypothesis \mathcal{H}_j under the observed data \mathcal{D} (Knuth et al., 2015).

Translating this into practice, after training the emulators, given an observed signal \mathcal{D} as described in Sect. 3.3, we can com-

pare the three following equiprobable hypotheses: the source mechanism is isotropic (\mathcal{H}_{ISO}), the source mechanism is double couple (\mathcal{H}_{DC}), or the source mechanism is compensated linear vector dipole ($\mathcal{H}_{\text{CLVD}}$). The advantage of using nested sampling is that the evidence is calculated while sampling the posterior distribution. Consequently, by feeding the observation \mathbf{D} to each emulator it is straightforward to obtain the evidences $\Pr(\mathbf{D}|\mathcal{H}_{\text{ISO}})$, $\Pr(\mathbf{D}|\mathcal{H}_{\text{DC}})$ and $\Pr(\mathbf{D}|\mathcal{H}_{\text{CLVD}})$. By looking at the hypothesis that maximises the evidence, we can select the model that best describes the given observation, thus identifying the source type for a given observation. We show the results in Sect. 4.3 and Table 2.

4 RESULTS

4.1 Speed performance

We first report on the speed performance of our method. We recall here that if we were to solve the elastic wave equation at each likelihood evaluation, inference would be severely compromised, as a single event's source inversion would take thousands of hours on a High Performance Computing (HPC) cluster, if at all possible. In contrast, our method requires only $\sim 10^4$ simulations to be produced once - an overhead of $\mathcal{O}(100 \text{ h})$ - and then it allows for the complete source inversion of any event in $\mathcal{O}(1 \text{ h})$ on a commercial laptop. More importantly, perhaps, most of this time is spent training the emulator, which needs to be done only once as well, provided the density and velocity models remain unchanged[§]; after the training is complete, performing inference on a given recorded seismogram takes $\mathcal{O}(0.1 \text{ h})$ on the same commercial laptop.

4.2 Inference results

We then turn our attention to the accuracy of the inferred posterior distribution of the coordinates. For each source mechanism, we report the inference results for 3 different coordinates in Figs. 6, 7 and 8: each shows the posterior contour plots obtained with our methodology, considering all 23 receivers, SNR=33 dB and using 8000 seismograms as the training set for the emulator. The numerical results are summarised in Table 1, reporting the prior ranges and marginalised mean and 68 percent credibility interval on the coordinates. We note that with our method we can accurately retrieve the correct value of the coordinates across the prior parameter space, as our results always match the events' coordinates within error bars. Additionally, we note that the x and y coordinates are usually less constrained than the z coordinate for ISO and CLVD, while this behaviour is less prominent in the DC case, for which all coordinates are always tightly constrained. We attribute this effect to two possible causes. On one hand, it can be related to the specific density model we are considering in this work, which has a layered structure. On the other hand, we note that when translating the seismic traces to the Fourier domain we ignored the phase signal (since we only considered the power spectra), thus possibly losing useful information for the localisation purpose (Ferreira and Woodhouse, 2007). We additionally note that retaining the phase information would yield a generative model, as by combining the power spectra with the phase one could in principle reconstruct a

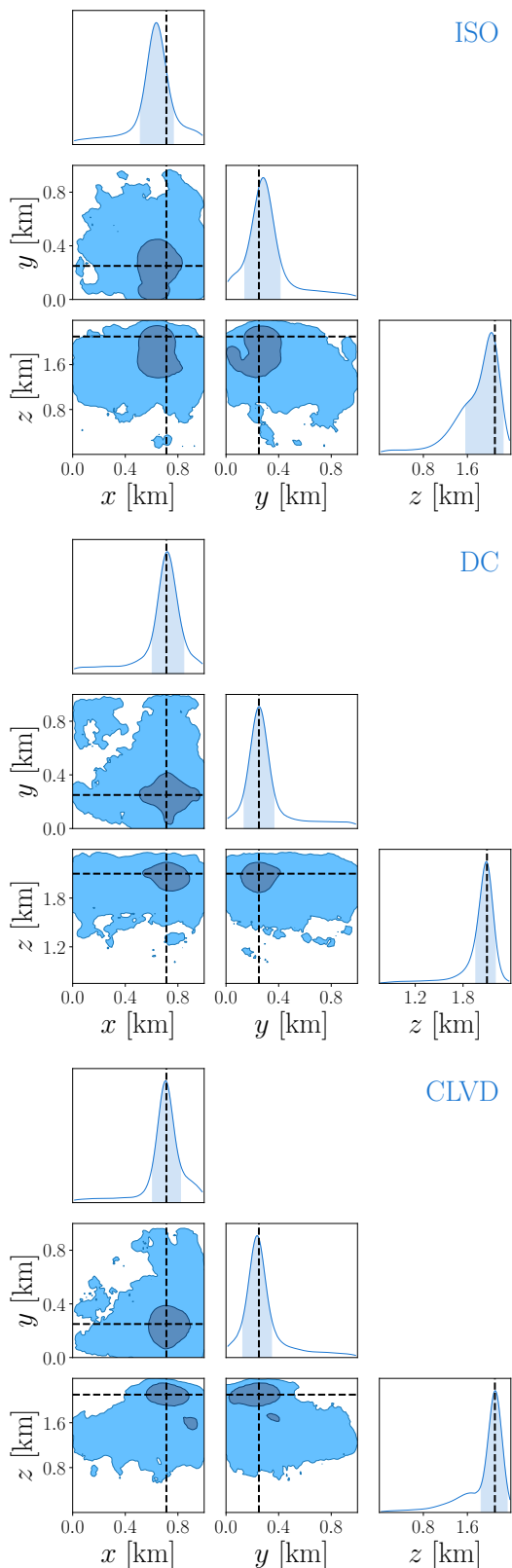


Figure 6. Marginalised 68 and 95 per cent credibility contours obtained with our method for a source located at $(x, y, z) = (0.71 \text{ km}, 0.25 \text{ km}, 2.10 \text{ km})$, indicated by the black dashed lines. We compare 3 source mechanisms: isotropic (ISO), double couple (DC), and compensated linear vector dipole (CLVD). The event corresponds to event 1 in Table 1. Note that we are considering 23 receivers, the signal-to-noise ratio is 33 dB and the emulator was trained on 8000 training points.

[§] In general, the stability of a given velocity model is not well known - see e.g. Thornton (2013); Usher et al. (2013); Gesret et al. (2013, 2014); Das et al. (2018) and references therein for a discussion on the uncertainties of velocity models, and their consequences on location errors.

Event	Coordinate	Prior range [km]	Ground truth [km]	ISO [km]	DC [km]	CLVD [km]
1	x	[0, 1]	0.71	$0.63^{+0.13}_{-0.12}$	$0.72^{+0.13}_{-0.11}$	$0.71^{+0.11}_{-0.10}$
	y	[0, 1]	0.25	$0.28^{+0.13}_{-0.14}$	$0.25^{+0.10}_{-0.11}$	$0.24^{+0.11}_{-0.11}$
	z	[0, 2.43]	2.10	$2.04^{+0.21}_{-0.47}$	$2.09^{+0.11}_{-0.13}$	$2.10^{+0.22}_{-0.25}$
2	x	[0, 1]	0.46	$0.48^{+0.19}_{-0.19}$	$0.43^{+0.12}_{-0.13}$	$0.46^{+0.15}_{-0.12}$
	y	[0, 1]	0.34	$0.32^{+0.16}_{-0.19}$	$0.33^{+0.09}_{-0.08}$	$0.33^{+0.15}_{-0.14}$
	z	[0, 2.43]	1.48	$1.60^{+0.23}_{-0.30}$	$1.54^{+0.18}_{-0.15}$	$1.44^{+0.22}_{-0.24}$
3	x	[0, 1]	0.20	$0.28^{+0.20}_{-0.15}$	$0.20^{+0.10}_{-0.10}$	$0.22^{+0.25}_{-0.13}$
	y	[0, 1]	0.43	$0.46^{+0.18}_{-0.16}$	$0.41^{+0.10}_{-0.13}$	$0.54^{+0.17}_{-0.21}$
	z	[0, 2.43]	0.99	$0.93^{+0.17}_{-0.19}$	$1.09^{+0.28}_{-0.17}$	$0.98^{+0.21}_{-0.20}$

Table 1. Prior range and marginalised mean and 68 percent credibility intervals on the coordinates (x, y, z), for each source mechanism - isotropic (ISO), double couple (DC) and compensated linear vector dipole (CLVD). The three events are randomly sampled from the test set. These results are obtained by considering all 23 receivers, and training on 8000 simulated events. The noise level is set to 10.0, 0.3 and 3.5 respectively, which corresponds to a signal-to-noise ratio of 33 dB.

Event type	$\ln \Pr(D \mathcal{H}_{\text{ISO}})$	$\ln \Pr(D \mathcal{H}_{\text{DC}})$	$\ln \Pr(D \mathcal{H}_{\text{CLVD}})$
ISO	2601	-608	-79
DC	-17688	-1165	-2232
CLVD	-6620	-1052	-394

Table 2. Natural logarithm of the evidence for a source located at $(x, y, z) = (0.71 \text{ km}, 0.25 \text{ km}, 2.10 \text{ km})$ and source mechanism isotropic (ISO), double couple (DC) and compensated linear vector dipole (CLVD), as described in Sect. 3.4 and Sect. 4.3. The hypotheses correspond to an ISO (\mathcal{H}_{ISO}), DC (\mathcal{H}_{DC}) and CLVD ($\mathcal{H}_{\text{CLVD}}$) source mechanism, respectively. We highlighted in bold the highest evidence in each line, which correctly corresponds to the known source mechanism. Note that the natural logarithm of the evidence is returned by PYMULTINEST, and in this instance we ignored its associated error (which is very small).

full seismogram from the coordinates (after training the emulator). We defer the study of phase information to future work, as we anticipate that given the oscillatory behaviour of the phase signals it will be harder to train an emulator on them.

We then study the dependence of the posterior contours on the SNR, the number of training data and the number of receivers used. In Fig. 9, we first show the effect of different noise levels; in particular, for each source mechanism we vary the SNR from 13 dB to 54 dB. We note that, in order to increase the robustness to noise, we cut different frequency windows based on the noise levels: given the Gaussian noise model we assume in this work, a smaller SNR corresponds to a higher noise power, and hence to a smaller number of retained power spectrum components. We observe that while higher noise levels can lead to small biases in some of the 1D marginalised coordinates' distributions, in general no significant variations in the shape of the 2-D posterior contours are present.

In Fig. 10 we show the posterior contours when training the emulator with 2000, 5000 and 8000 data points. Again, we observe no significant differences for the ISO and CLVD sources, while very small deviations appear when using fewer training data in the DC case. In general, $\mathcal{O}(10^3)$ training data are enough to obtain accurate posterior contours for all source mechanisms. Finally, in Fig. 11 we vary the geometry of the receivers used for recording the microseismic traces. While we are not interested in a full study of the optimal geometry of the receivers, we observe that using fewer receivers leads to broader posterior contours, while still allowing for the accurate localisation of the event for all source mechanisms.

In summary, our results are very robust to the noise injected

into the observed seismogram. Additionally, very few receivers - $\mathcal{O}(10)$ - are needed to obtain accurate results, and a number of training points of order $\mathcal{O}(10^3)$ is sufficient to localise any event.

4.3 Model selection results

In general, a real event can be described as a linear combination of the three source mechanisms described in Sect. 2 (Vavryčuk, 2015). While we considered the three sources separately in this work, we show how the proposed Bayesian approach additionally allows for the identification of a source type given an observed seismogram. We consider event 1 as reported in Table 1, and produce an observation for each source mechanism (ISO, DC and CLVD). As described in Sect. 3.4, we can run nested sampling for each event and for every trained emulator, and obtain 9 evidence values in total, whose logarithm we report in Table 2. As expected, the evidence is maximal in correspondence of the source type that generated the given event, which indicates that we are capable of correctly identifying the source type for a given observation. What is more, this selection is also very fast, as after training the emulators each evidence calculation takes less than 10 minutes on a commercial laptop.

5 CONCLUSIONS

In this paper, we proposed a method that allows for the fast and accurate retrieval of the coordinates for any microseismic source mechanism: isotropic (ISO), double couple (DC), and compensated linear vector dipole (CLVD). This offers an efficient technique to both localise an event and identify its source type, exploiting the power of machine learning and Bayesian tools to extract the information contained in the seismic waveforms.

Our proposed method is based on a physically motivated pre-processing of the raw signals, using Fourier analysis and principal component compression, followed by the use of a neural network to learn the mapping between coordinates and principal components. Using the learnt forward model in combination with Bayesian techniques, we showed that we can retrieve an accurate estimate of any microseismic event coordinates, for any source mechanism, in less than 1 hour on a commercial laptop. Therefore, we demonstrated for the first time that machine learning techniques allow for a fast and accurate Bayesian analysis on microseismic traces, yielding

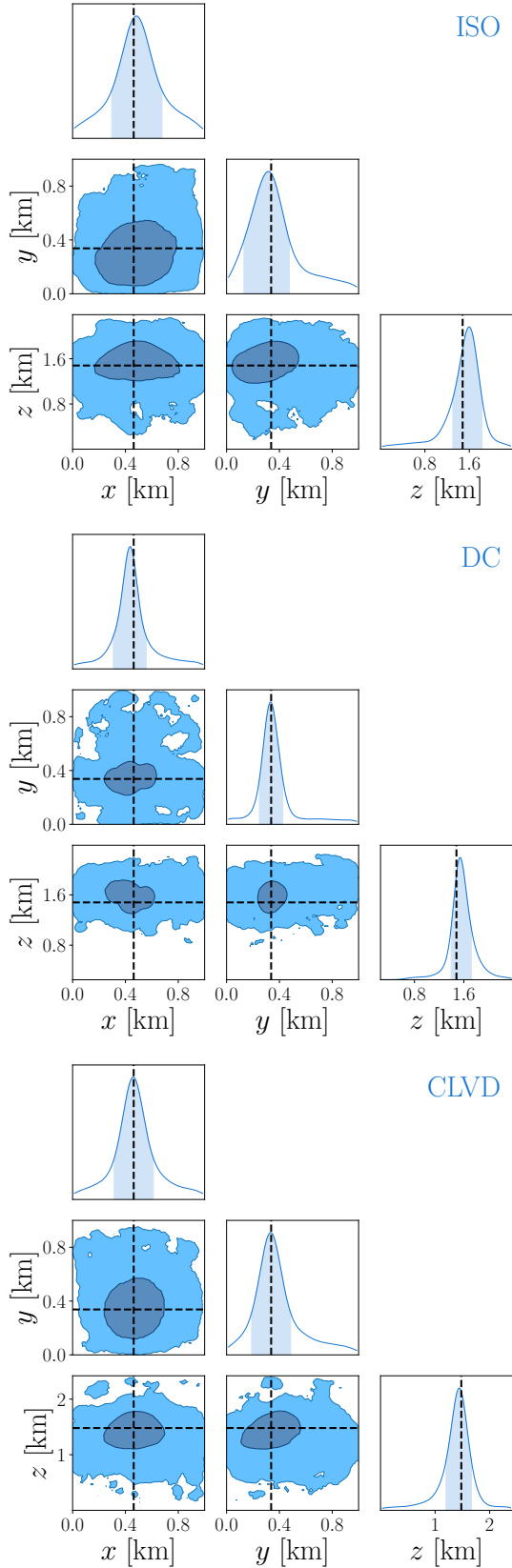


Figure 7. Same as Fig. 6 for a source located at $(x, y, z) = (0.46 \text{ km}, 0.34 \text{ km}, 1.48 \text{ km})$. The event corresponds to event 2 in Table 1.

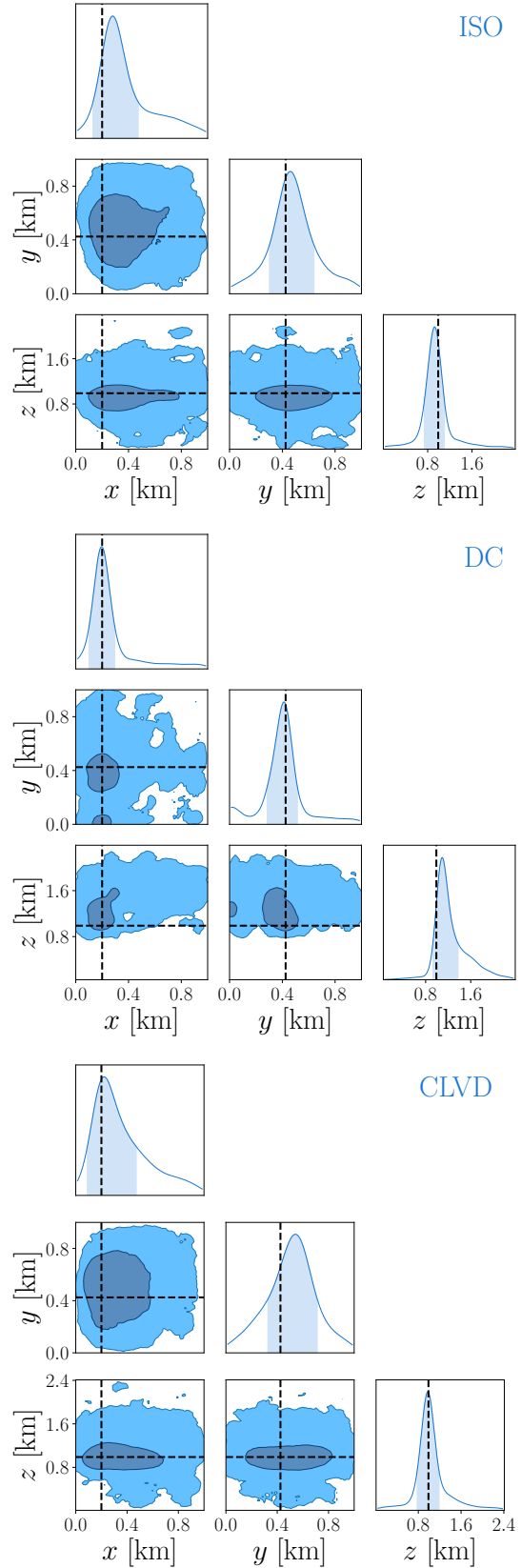


Figure 8. Same as Fig. 6 for a source located at $(x, y, z) = (0.20 \text{ km}, 0.43 \text{ km}, 0.99 \text{ km})$. The event corresponds to event 3 in Table 1.

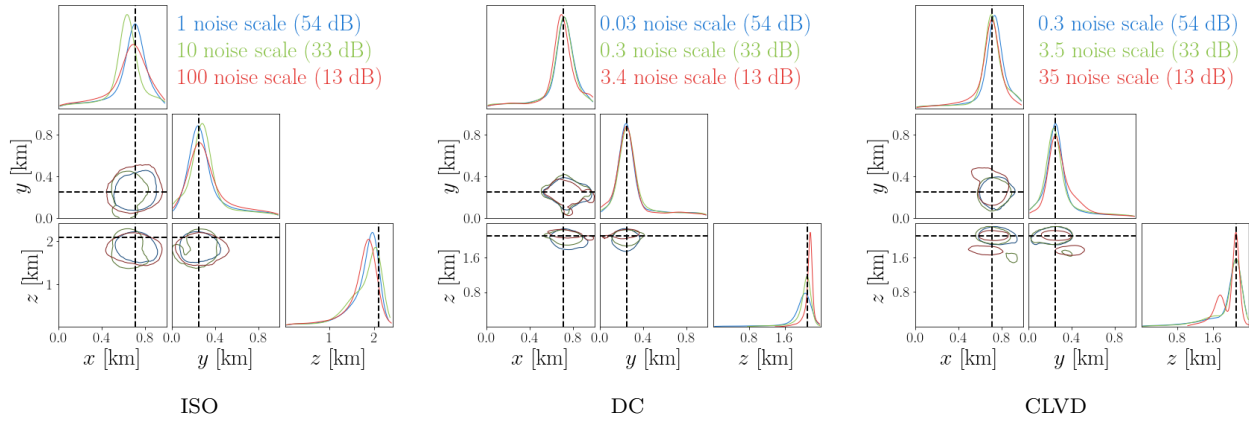


Figure 9. Marginalised 68 per cent credibility contours obtained with our method for a source located at $(x, y, z) = (0.71 \text{ km}, 0.25 \text{ km}, 2.10 \text{ km})$, indicated by the black dashed lines, comparing different levels of noise. In particular, in each panel we show signal-to-noise ratios of 13 dB, 33 dB and 54 dB for the 3 source mechanisms: isotropic (ISO), double couple (DC), and compensated linear vector dipole (CLVD). Note that we are considering 8000 training data for the emulator and 23 receivers.

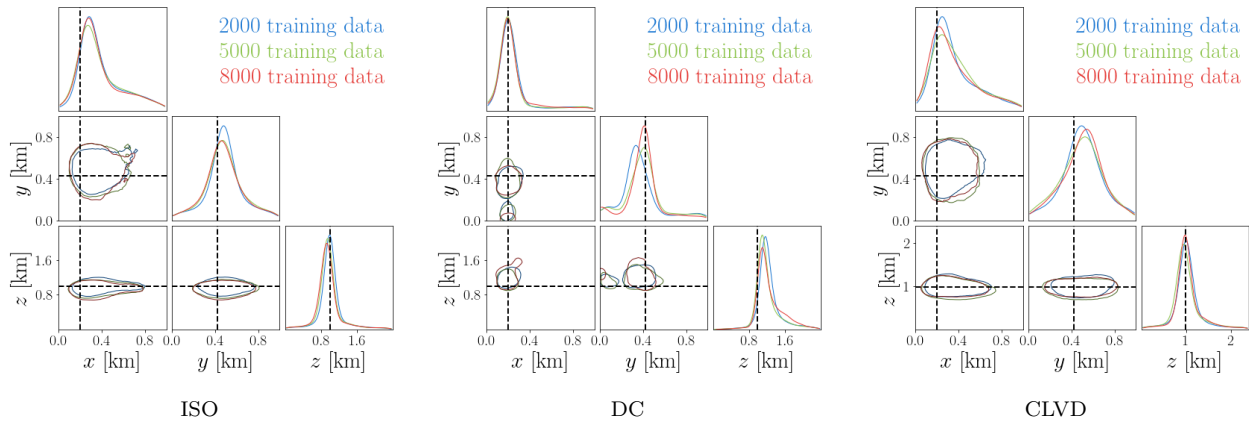


Figure 10. Marginalised 68 per cent credibility contours obtained with our method for a source located at $(x, y, z) = (0.20 \text{ km}, 0.43 \text{ km}, 0.99 \text{ km})$, indicated by the black dashed lines, comparing different numbers of training data for the emulator (2000, 5000 and 8000). We show these results for 3 source mechanisms: isotropic (ISO), double couple (DC), and compensated linear vector dipole (CLVD). Note that we are considering 23 receivers and a signal-to-noise ratio of 33 dB.

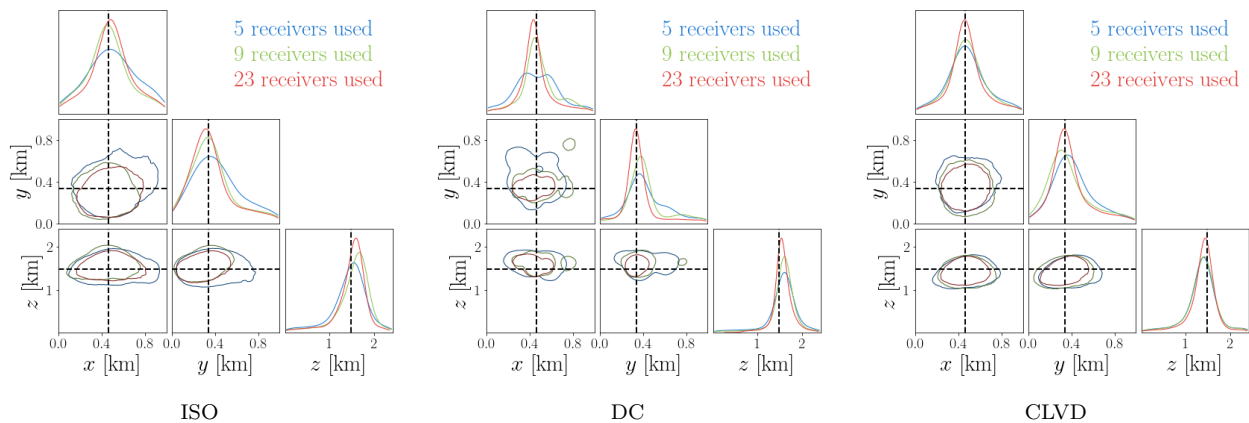


Figure 11. Marginalised 68 per cent credibility contours obtained with our method for a source located at $(x, y, z) = (0.46 \text{ km}, 0.34 \text{ km}, 1.48 \text{ km})$, indicated by the black dashed lines, comparing different dispositions of the receivers. In particular, 5 receivers refer to the blue squares in Fig. 2, and 9 receivers refer to the green circles in Fig. 2. We show these results for 3 source mechanisms: isotropic (ISO), double couple (DC), and compensated linear vector dipole (CLVD). Note that we are considering 8000 training data for the emulator and a signal-to-noise ratio of 33 dB.

competitive results on ISO sources and state-of-the-art results on DC and CLVD sources.

We showed that $\mathcal{O}(10^3)$ events for each source mechanism are enough to train a representative emulator, when using the data coming from $\mathcal{O}(10)$ receivers placed at the seabed as indicated in Fig. 2. We also explored the effect of the noise level, and how the number of receivers and the number of training data for the emulator impact the accuracy of the coordinates' posterior distribution, demonstrating the robustness of our approach. Finally, we demonstrated the utility of our Bayesian approach by calculating the Bayesian evidence for a given observation and three hypotheses, and showed that this correctly identifies the source type of any given event.

In conclusion, our work lays the foundations for the fast and reliable localisation of any microseismic event, given a minimal amount of computing resources. Some straightforward extensions of our method include the following three points. First, we note that in order for this method to be deployed in a realistic scenario, the noise associated with the recorded sesimograms should be modelled more carefully: a lower SNR may have to be considered, a more complicated likelihood distribution might have to be implemented, or a “likelihood-free” approach should be investigated (Sunnåker et al., 2013). Second, the errors in the 3-D density and velocity models should be incorporated into the analysis, in order to account for all sources of uncertainty (Gesret et al., 2013, 2014). Last, a real microseismic event is in general described by a linear mixture of components of the moment tensor, which we considered separately in this work. This increases the total number of parameters to infer, which we anticipate will require a larger dataset to train the emulator. However, we note that our proposed method scales well with the number of training data, and therefore we speculate that performing a Bayesian analysis with a larger parameter space is an attainable goal using our approach. This will be addressed in future work, while the code to reproduce this work will be made publicly available in the GitHub repository at this link[¶] upon acceptance of the paper.

ACKNOWLEDGMENTS

We thank Saptarshi Das and Ana Ferreira for useful discussions. DP is supported by the STFC UCL Centre for Doctoral Training in Data Intensive Science. Generation of the synthetic data used in this work has been performed in part on the Wilkes High Performance GPU computer cluster at the University of Cambridge, and in part on the Beaker cluster at UCL. This work has been partially enabled by funding from Royal Dutch Shell plc and the UCL Cosmoparticle Initiative. We acknowledge the use of NUMPY (Harris et al., 2020), MATPLOTLIB (Hunter, 2007), TENSORFLOW (Abadi et al., 2015), SCIPY (Virtanen et al., 2020), and CHAINCONSUMER (Hinton, 2016).

References

- Abadi, M., Agarwal, A., Barham, P., Brevdo, E., Chen, Z., Citro, C., Corrado, G. S., Davis, A., Dean, J., Devin, M., Ghemawat, S., Goodfellow, I., Harp, A., Irving, G., Isard, M., Jia, Y., Jozefowicz, R., Kaiser, L., Kudlur, M., Levenberg, J., Mané, D., Monga, R., Moore, S., Murray, D., Olah, C., Schuster, M., Shlens, J., Steiner, B., Sutskever, I., Talwar, K., Tucker, P., Vanhoucke, V., Vasudevan, V., Viégas, F., Vinyals, O., Warden, P., Wattenberg, M., Wicke, M., Yu, Y., and Zheng, X. (2015). TensorFlow: Large-scale machine learning on heterogeneous systems. Software available from tensorflow.org.
- Allison, R. and Dunkley, J. (2014). Comparison of sampling techniques for Bayesian parameter estimation. *Mon. Not. Roy. Astron. Soc.*, 437(4):3918–3928.
- Alsing, J., Wandelt, B., and Feeney, S. (2018). Massive optimal data compression and density estimation for scalable, likelihood-free inference in cosmology. *Mon. Not. Roy. Astron. Soc.*, 477(3):2874–2885.
- Angus, D., Aljaafari, A., Usher, P., and Verdon, J. (2014). Seismic waveforms and velocity model heterogeneity: Towards a full-waveform microseismic location algorithm. *Journal of Applied Geophysics*, 111:228 – 233.
- Auld, T., Bridges, M., Hobson, M., and Gull, S. (2007). Fast cosmological parameter estimation using neural networks. *Mon. Not. Roy. Astron. Soc.*, 376:L11–L15.
- Auld, T., Bridges, M., and Hobson, M. P. (2008). cosmonet: fast cosmological parameter estimation in non-flat models using neural networks. *Monthly Notices of the Royal Astronomical Society*, 387(4):1575–1582.
- Bishop, C. M. (2006). *Pattern Recognition and Machine Learning (Information Science and Statistics)*. Springer-Verlag, Berlin, Heidelberg.
- Brueckl, E., Binder, D., Hausmann, H., and Mertl, S. (2008). Hazard Estimation of Deep Seated Mass Movements by Microseismic Monitoring. In *International Strategy for Disaster Reduction*.
- Buchner, J., Georgakakis, A., Nandra, K., Hsu, L., Rangel, C., Brightman, M., Merloni, A., Salvato, M., Donley, J., and Kocevski, D. (2014). X-ray spectral modelling of the AGN obscuring region in the CDFS: Bayesian model selection and catalogue. *AAP*, 564:A125.
- Chenthamarakshan, V., Das, P., Hoffman, S. C., Strobelt, H., Padhi, I., Lim, K. W., Hoover, B., Manica, M., Born, J., Laino, T., and Mojsilovic, A. (2020). CogMol: Target-Specific and Selective Drug Design for COVID-19 Using Deep Generative Models. *arXiv e-prints*, page arXiv:2004.01215.
- Collettini, C. and Barchi, M. R. (2002). A low-angle normal fault in the Umbria region (Central Italy): a mechanical model for the related microseismicity. *Tectonophysics*, 359(1):97 – 115.
- Conrad, P. R., Marzouk, Y. M., Pillai, N. S., and Smith, A. (2016). Accelerating Asymptotically Exact MCMC for Computationally Intensive Models via Local Approximations. *Journal of the American Statistical Association*, 111(516):1591–1607.
- Cooley, J. W. and Tukey, J. W. (1965). An Algorithm for the Machine Calculation of Complex Fourier Series. *Math. Comput.*, 19:297–301.
- Craiu, R. V. and Rosenthal, J. S. (2014). Bayesian Computation via Markov Chain Monte Carlo. *Annual Review of Statistics and Its Application*, 1(1):179–201.
- Das, S., Chen, X., and Hobson, M. P. (2017). Fast GPU-Based Seismogram Simulation From Microseismic Events in Marine Environments Using Heterogeneous Velocity Models. *IEEE Transactions on Computational Imaging*, 3(2):316–329.
- Das, S., Chen, X., Hobson, M. P., Phadke, S., van Beest, B., Goudswaard, J., and Hohl, D. (2018). Surrogate regression modelling for fast seismogram generation and detection of microseismic events in heterogeneous velocity models. *Geophysical Journal International*, 215(2):1257–1290.

¶ <https://github.com/alessiospuriomancini/seismoML>

- Ellsworth, W. L. (2013). Injection-induced earthquakes. *Science*, 341(6142).
- Feroz, F., Hobson, M., and Bridges, M. (2009). MultiNest: an efficient and robust Bayesian inference tool for cosmology and particle physics. *Mon. Not. Roy. Astron. Soc.*, 398:1601–1614.
- Ferreira, A. M. G. and Woodhouse, J. H. (2007). Source, path and receiver effects on seismic surface waves. *Geophysical Journal International*, 168(1):109–132.
- Fertitta, G., Stefano, A. D., Fiscelli, G., and Giaconia, G. C. (2010). A low power and high resolution data logger for submarine seismic monitoring. *Microprocessors and Microsystems*, 34(2):63–72.
- Geiger, L. (1910). Herdbestimmung bei Erdbeben aus den Ankunftszeiten, Nachrichten der K. Gesellschaft der Wissenschaften zu Göttingen. *Math.-Phys. Klasse*, pages 331–349.
- Gesret, A., Desassis, N., Noble, M., Romary, T., and Maisons, C. (2014). Propagation of the velocity model uncertainties to the seismic event location. *Geophysical Journal International*, 200(1):52–66.
- Gesret, A., Noble, M., Desassis, N., and Romary, T. (2013). Microseismic Monitoring - Consequences of Velocity Model Uncertainties on Event Location Uncertainties. *Proceedings of the Third Passive Seismic Workshop, Eur. Ass. of Geoscientists and Engineers, Athens - Greece (2011)*.
- Goodfellow, I., Pouget-Abadie, J., Mirza, M., Xu, B., WardeFarley, D., Ozair, S., Courville, A., and Bengio, Y. (2014). Generative Adversarial Nets. In Ghahramani, Z., Welling, M., Cortes, C., Lawrence, N. D., and Weinberger, K. Q., editors, *Advances in Neural Information Processing Systems 27*, pages 2672–2680. Curran Associates, Inc.
- Gulrajani, I., Kumar, K., Ahmed, F., Taiga, A. A., Visin, F., Vazquez, D., and Courville, A. (2016). PixelVAE: A Latent Variable Model for Natural Images. *arXiv e-prints*, page arXiv:1611.05013.
- Harris, C. R., Millman, K. J., van der Walt, S. J., Gommers, R., Virtanen, P., Cournapeau, D., Wieser, E., Taylor, J., Berg, S., Smith, N. J., Kern, R., Picus, M., Hoyer, S., van Kerkwijk, M. H., Brett, M., Haldane, A., del Río, J. F., Wiebe, M., Peterson, P., Gérard-Marchant, P., Sheppard, K., Reddy, T., Weckesser, W., Abbasi, H., Gohlke, C., and Oliphant, T. E. (2020). Array programming with NumPy. *Nature*, 585(7825):357–362.
- Haykin, S. (2001). *Communication Systems*. Wiley.
- Hinton, S. R. (2016). ChainConsumer. *The Journal of Open Source Software*, 1:00045.
- Hornik, K., Stinchcombe, M., and White, H. (1989). Multilayer feedforward networks are universal approximators. *Neural Networks*, 2(5):359–366.
- Hunter, J. D. (2007). Matplotlib: A 2d graphics environment. *Computing in Science & Engineering*, 9(3):90–95.
- Kasim, M. F., Watson-Parris, D., Deaconu, L., Oliver, S., Hatfield, P., Froula, D. H., Gregori, G., Jarvis, M., Khatiwala, S., Korenaga, J., Topp-Muggleston, J., Viezzer, E., and Vinko, S. M. (2020). Building high accuracy emulators for scientific simulations with deep neural architecture search.
- Kingma, D. P. and Ba, J. (2014). Adam: A Method for Stochastic Optimization.
- Knopoff, L. and Randall, M. J. (1970). The compensated linear-vector dipole: A possible mechanism for deep earthquakes. *Journal of Geophysical Research (1896-1977)*, 75(26):4957–4963.
- Knuth, K. H., Habeck, M., Malakar, N. K., Mubeen, A. M., and Placek, B. (2015). Bayesian evidence and model selection. *Digital Signal Processing*, 47:50–67. Special Issue in Honour of William J. (Bill) Fitzgerald.
- Kolen, J. F. and Kremer, S. C. (2001). *Gradient Flow in Recurrent Nets: The Difficulty of Learning LongTerm Dependencies*, pages 237–243. Wiley-IEEE Press.
- Li, H., Wang, R., and Cao, S. (2015). Microseismic forward modeling based on different focal mechanisms used by the seismic moment tensor and elastic wave equation. *Journal of Geophysics and Engineering*, 12(2):155–166.
- Li, J., Ji, S., Li, Y., Qian, Z., and Lu, W. (2018). Downhole microseismic signal-to-noise ratio enhancement via strip matching shearlet transform. *Journal of Geophysics and Engineering*, 15(2):330–337.
- Liu, E., Zhu, L., Govinda Raj, A., McClellan, J. H., Al-Shuhail, A., Kaka, S. I., and Iqbal, N. (2017). Microseismic events enhancement and detection in sensor arrays using autocorrelation-based filtering. *Geophysical Prospecting*, 65(6):1496–1509.
- Liu, H., Ong, Y.-S., Shen, X., and Cai, J. (2018). When Gaussian Process Meets Big Data: A Review of Scalable GPs. *arXiv e-prints*, page arXiv:1807.01065.
- Lomax, A., Virieux, J., Volant, P., and Berge-Thierry, C. (2000). *Probabilistic Earthquake Location in 3D and Layered Models*, pages 101–134. Springer Netherlands, Dordrecht.
- Maas, A. L., Hannun, A. Y., and Ng, A. Y. (2013). Rectifier nonlinearities improve neural network acoustic models. In *ICML Workshop on Deep Learning for Audio, Speech and Language Processing*.
- Majer, E. L., Baria, R., Stark, M., Oates, S., Bommer, J., Smith, B., and Asanuma, H. (2007). Induced seismicity associated with Enhanced Geothermal Systems. *Geothermics*, 36(3):185–222.
- Mukuhira, Y., Asanuma, H., Ito, T., and Häring, M. O. (2016). Physics-based seismic evaluation method: Evaluating possible seismic moment based on microseismic information due to fluid stimulation. *GEOPHYSICS*, 81(6):KS195–KS205.
- Noack, M. M. and Clark, S. (2017). Acoustic wave and eikonal equations in a transformed metric space for various types of anisotropy. *Heliyon*, 3(3):e00260.
- Panahi, S. S., Ventosa, S., Cadena, J., Manuel, A., Bermudez, T., Sallares, V., Piera, J., and Del Rio, J. (2005). A Low Power Datalogger based on Compactflash memory for Ocean Bottom Seismometers (obs). In *2005 IEEE Instrumentation and Measurement Technology Conference Proceedings*, volume 2, pages 1278–1281.
- Papoulis, A., Pillai, S., and Pillai, S. (2002). *Probability, Random Variables, and Stochastic Processes*. McGraw-Hill electrical and electronic engineering series. McGraw-Hill.
- Pugh, D. J., White, R. S., and Christie, P. A. F. (2016). A Bayesian method for microseismic source inversion. *Geophysical Journal International*, 206(2):1009–1038.
- Rajaratnam, B. and Sparks, D. (2015). MCMC-Based Inference in the Era of Big Data: A Fundamental Analysis of the Convergence Complexity of High-Dimensional Chains. *arXiv e-prints*, page arXiv:1508.00947.
- Rasmussen, C. E. and Williams, C. K. I. (2005). *Gaussian Processes for Machine Learning (Adaptive Computation and Machine Learning)*. The MIT Press.
- Shapiro, S. A., Dinske, C., Langenbruch, C., and Wenzel, F. (2010). Seismogenic index and magnitude probability of earthquakes induced during reservoir fluid stimulations. *The Leading Edge*, 29(3):S. 304–309.
- Skilling, J. (2006). Nested sampling for general Bayesian computation. *Bayesian Analysis*, 1(4):833–859.
- Smith, J. D., Azizzadenesheli, K., and Ross, Z. E. (2020).

- EikoNet: Solving the Eikonal equation with Deep Neural Networks. *arXiv e-prints*, page arXiv:2004.00361.
- Spurio Mancini, A., Piras, D., Hobson, M. P., and Joachimi, B. (2020). Deep generative models for accelerated Bayesian posterior inference of microseismic events. *arXiv e-prints*, page arXiv:2009.06758.
- Stähler, S. C. and Sigloch, K. (2014). Fully probabilistic seismic source inversion – part 1: Efficient parameterisation. *Solid Earth*, 5(2):1055–1069.
- Stähler, S. C. and Sigloch, K. (2016). Fully probabilistic seismic source inversion – part 2: Modelling errors and station covariances. *Solid Earth*, 7(6):1521–1536.
- Sunnåker, M., Busetto, A. G., Numminen, E., Corander, J., Foll, M., and Dessimoz, C. (2013). Approximate Bayesian Computation. *PLoS Computational Biology*, 9(1):1–10.
- Tarantola, A. (2005). *Inverse Problem Theory and Methods for Model Parameter Estimation*. Society for Industrial and Applied Mathematics.
- Thornton, M. (2013). Velocity uncertainties in surface and down-hole monitoring. *Conference Proceedings, 4th EAGE Passive Seismic Workshop*.
- Treeby, B. E., Jaros, J., Rohrbach, D., and Cox, B. T. (2014). Modelling elastic wave propagation using the k-Wave MATLAB Toolbox. In *2014 IEEE International Ultrasonics Symposium*, pages 146–149.
- Usher, P., Angus, D., and Verdon, J. (2013). Influence of a velocity model and source frequency on microseismic waveforms: some implications for microseismic locations. *Geophysical Prospecting*, 61(s1):334–345.
- Vasco, D. W., Nakagawa, S., Petrov, P., and Newman, G. (2019). Rapid estimation of earthquake locations using waveform traveltimes. *Geophysical Journal International*, 217(3):1727–1741.
- Vavryčuk, V. (2015). Moment tensor decompositions revisited. *Journal of Seismology*, 19(1):231–252.
- Vavryčuk, V. (2001). Inversion for parameters of tensile earthquakes. *Journal of Geophysical Research: Solid Earth*, 106(B8):16339–16355.
- Vavryčuk, V. (2005). Focal mechanisms in anisotropic media. *Geophysical Journal International*, 161(2):334–346.
- Virtanen, P., Gommers, R., Oliphant, T. E., Haberland, M., Reddy, T., Cournapeau, D., Burovski, E., Peterson, P., Weckesser, W., Bright, J., van der Walt, S. J., Brett, M., Wilson, J., Millman, K. J., Mayorov, N., Nelson, A. R. J., Jones, E., Kern, R., Larson, E., Carey, C. J., Polat, İ., Feng, Y., Moore, E. W., VanderPlas, J., Laxalde, D., Perktold, J., Cimrman, R., Henriksen, I., Quintero, E. A., Harris, C. R., Archibald, A. M., Ribeiro, A. H., Pedregosa, F., van Mulbregt, P., and SciPy 1.0 Contributors (2020). SciPy 1.0: Fundamental Algorithms for Scientific Computing in Python. *Nature Methods*, 17:261–272.
- Wuestefeld, A., Greve, S. M., Näsholm, S. P., and Oye, V. (2018). Benchmarking earthquake location algorithms: A synthetic comparison. *Geophysics*, 83(4):KS35–KS47.
- Yao, Y., Rosasco, L., and Caponnetto, A. (2007). On Early Stopping in Gradient Descent Learning. *Constructive Approximation*, 26:289–315.
- Zhang, J., Dong, L., and Xu, N. (2020). Noise Suppression of Microseismic Signals via Adaptive Variational Mode Decomposition and Akaike Information Criterion. *Applied Sciences*, 10(11):3790.
- Zhu, X., Vondrick, C., Fowlkes, C., and Ramanan, D. (2015). Do We Need More Training Data? *arXiv e-prints*, page arXiv:1503.01508.